Modelling acid attack of oilwell cement exposed to carbonated brine

Joaquín Liaudat*, Ariadna Martínez, Carlos M. López, Ignacio Carol

ETSECCPB (School of Civil Engineering), UPC (Technical Univ. of Catalonia), Jordi Girona 1, Edif. D2, E-08034 Barcelona.

A B S T R A C T

A diffusion-reaction model for the carbonation process of oilwell cement exposed to carbonated brine under CO_2 geological storage conditions is presented. The formulation consists of two main diffusion/reaction field equations for the concentrations of aqueous calcium and carbon species in the pore solution of the hardened cement paste, complemented by two diffusion-only field equations for chloride and alkalis concentrations, and by a number of chemical kinetics and chemical equilibrium equations. The volume fraction distribution of the solid constituents of the hardened cement paste and the reaction products evolve with the progress of the reaction, determining the diffusivity properties of the material. The model is used to simulate experimental tests performed by Duguid & Scherer (2010), leading to promising results indicating that the fundamental aspects of the phenomenon are captured.

Keywords: Carbonation, Carbon sequestration, Well cement, CO_2, Carbonic acid, Chemical model, Finite Element Method

1. Introduction

Capture and geological storage of CO_2 are intended to avoid emitting CO_2 into the atmosphere, by capturing CO_2 from major stationary sources (thermal power plants, cement factories, etc.), transporting it usually by pipeline and injecting it into suitable deep rock formations (IPCC, 2005). Among other possibilities (e.g. saline formations, coal formations), CO_2 storage in depleted oil and gas reservoirs is very promising, first, because the oil and gas that originally accumulated in traps did not escape (in some cases for many millions of years), demonstrating their integrity and safety, and second, because these structures are well known and significant infrastructures are already in place. However, a major source of concern arises when the security of many mature oil fields for CO_2 storage is assessed: the presence of abandoned wells that perforate the cap rock of the reservoir and which may potentially constitute CO_2 leakage pathways. In many cases plugging of abandoned wells began decades ago when CO_2 storage was not under consideration and, so, the primary cement used for the casing, and/or the plug cement used in the well were regular Portland cements. If the resulting hydrated cement pastes (HCP) in the abandoned well gets in contact with the injected CO_2, two possible outcomes can be expected (Duguid and Scherer, 2010): (1) if the HCP is not submerged in water, a process similar to the carbonation of concrete in normal conditions will take place, with resulting slight increase of HCP strength and decrease of its permeability (Kutchko et al., 2008, 2007; Rimmelé et al., 2008); (2) if the HCP is submerged in water or brine, which is the most likely condition in an abandoned well in the long-term, it will suffer a progressive decalcification process, the so-called 'acid attack', which leads to a drastic loss of mechanical strength and increase of permeability (Carey et al., 2007; Duguid et al., 2011; Duguid and Scherer, 2010; Kutchko et al., 2008, 2007; Rimmelé et al., 2008; Walsh et al., 2013).

Potentially, acid attack may create leakage pathways through the well cement and worsen existing ones. Since redoing the abandoned wells cementation with acid resistant cements (e.g. calcium aluminate cements), even if possible at all, would be extremely expensive, one idea is clear: the acid attack can make more difficult, more expensive or even jeopardize the technical and economic feasibility of storing CO_2 in abandoned reservoir sites.

In this context, the potential benefits are evident of numerical models that make possible an accurate assessment of the long term performance of abandoned well cements when exposed to the injected CO_2.

In recent years, some models have been proposed. A detailed simulation of the cement paste degradation requires considering a large number of chemical species and reactions, as it has been proposed by Huet et al. (2010). However, for engineering purposes, satisfactory results can be obtained with simpler chemistry by omitting aluminium, iron and sulphur (solid and aqueous) species (Brunet et al., 2013; Fabbri et al., 2012; Raoof et al., 2012; Shen et al., 2013). One key aspect of the degradation process that due to its complexity is subject to simplification is the dissolution of C-S-H. It is well known that C-S-H presents an incongruent behaviour, i.e. the dissolution rate of the ions composing C-S-H is not proportional to the stoichiometric coefficient, and consequently, the composition of the C-S-H varies as the dissolution progresses. This incongruent behaviour is neglected by Huet et al. (2010) by emulating C-S-H gel as the crystalline mineral jennite and by Raoof et al. (2012) by directly omitting C-S-H dissolution. Shen et al. (2013) proposed an approach based on thermodynamics which leads to generalization of the mass action law for C-S-H with variable C/S ratio. This approach allows reproducing the incongruent dissolution of silicate and calcium ions. Other authors appealed to a less complex approach by simulating C-S-H dissolution as a multi-step process of decalcification passing from initial calcium-rich C-S-H (C/S=1.6-1.8) to intermediate C-S-H with lower calcium (Fabbri et al., 2012) or directly to amorphous silica (Brunet et al., 2013). Each of these intermediate compositions C-S-H is treated as a distinct mineral with fixed stoichiometry and solubility product constant. This approach allows those authors to approximate the incongruent dissolution behaviour without introducing any special treatment of C-S-H in comparison with the other solid species considered (e.g. portlandite or calcite).

The chemical model needs to be coupled to a transport model in order to simulate the ingress of carbon species and the egress of calcium. This coupling can be done via a monolithic formulation (fully coupled) (Brunet et al., 2013; Shen et al., 2013) or via an uncoupled formulation combined with an iterative procedure (staggered implementation) (Fabbri et al., 2012; Huet et al., 2010; Raoof et al., 2012). Staggered implementations allow easily combining pre-existent geochemical and transport codes, but exhibit the disadvantage of being only conditionally convergent, i.e. requiring small time steps to converge. On the other hand, fully coupled implementations converge much better but require important coding efforts.

*Corresponding author.

E-mail address: joaquin.liaudat@upc.edu (J. Liaudat)

Transport models may be divided in those which only consider transport of aqueous species through Fick's diffusion (Brunet et al., 2013; Huet et al., 2010), and those which also consider advective transport (Fabbri et al., 2012; Raoof et al., 2012; Shen, 2011). Since flow velocities through bulk cement paste is expected to be typically very slow under deep subsurface conditions, the effect of advective transport may be neglected in sound cements. However, in the case of cracked cements, the convective transport becomes dominant and needs to be considered in order to reproduce phenomena such the cracks widening or healing depending on flow rate of carbonated water (Huerta et al., 2016).

Besides the sink/source terms, coupling between chemical reactions and transport of aqueous species is also caused by the evolution of transport parameters such as porosity and effective diffusivity. The first is readily obtained from the volumetric balance of the solid species. Estimation of the effective diffusivity of the degraded HCP, in contrast, is not trivial. One usual approach is to consider the effective diffusivity to be a function of the porosity and one or more empirical parameters which remain constant (e.g. a power law in Huet et al. (2010) and Brunet et al. (2013) or an exponential law in Chen et al. (2013)). It must be noted that the parameters used with these laws were calibrated using cement pastes with different porosities due to different w/c ratios or age, but not with degraded pastes.

In the model presented in this paper, the emphasis has been made on keeping the formulation and the numerical implementation as simple as possible while reproducing the main aspects of the phenomenon, in particular those related with the degradation of the mechanical and transport properties.

2. The model

2.1. Reaction mechanism

The proposed reaction mechanism is schematically summarized in Fig. 1, which represents the interfacial zone between the HCP and the carbonated brine. The HCP is considered to be composed by four volumetric fractions: calcium silicate hydrates (C-S-H), free portlandite, inert cement hydrates, namely aluminate and sulphate compounds, and capillary pores. The HCP pores are assumed to be fully saturated with water with concentrations of alkalis (sodium and potassium) and chloride resultant from the cement hydration and from the exchange with the surrounding medium. These conditions, as well as the system pressure and temperature, are assumed to remain constant at all times during the reaction.

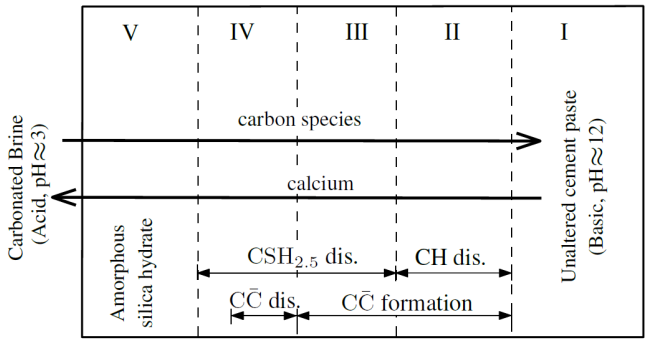

Fig. 1. Scheme of proposed carbonation mechanism. Note: CH=portlandite; C$\bar{C}$=calcite.

C-S-H is an amorphous gel with variable stoichiometry with averaged calcium to silica molar ratio around 1.70 for regular Portland cement. When exposed to an acid solution, degradation tends to lower the Ca/Si ratio, due to preferential release of Ca over Si (incongruent dissolution). A usual approach to model this incongruent dissolution behaviour is considering C-S-H as a solid solution of pure fixed-stoichiometry phases (components or end-members, with activity equal to 1) with defined saturation product constants (Börjesson et al., 1997; Rahman et al., 1999). In a similar way, we have considered C-S-H as a solid solution of hydrated silica gel and two fractions of portlandite, i.e.

$$(CaO)_{1.7}(SiO_2)(H_2O)_{3.2} \equiv \underbrace{[Ca(OH)_2]_{0.7}}_{A}\,\underbrace{[Ca(OH)_2]}_{B}\,[(SiO_2)(H_2O)_{1.5}]$$

Fraction A of portlandite is assumed to have the same solubility of free portlandite, and for all purposes it will be included in the free portlandite fraction considered in the model. In contrast, solubility of fraction B is assumed to be somewhat lower than that of free portlandite. Finally, for the sake of simplicity, silica gel is considered to be insoluble. Summarising, for modelling purposes, the C-S-H ($C_{1.7}SH_{3.2}$ in cement chemistry notation) is decomposed in two parts, on one hand, the 'free' portlandite (CH in cement chemistry notation) and, on the other, C-S-H with lower Ca/Si ratio ($CSH_{2.5}$ in cement chemistry notation), i.e. $C_{1.7}SH_{3.2} = 0.7CH + CSH_{2.5}$. Then, the C-S-H dissolution process can be represented in a simplified fashion by means of the reactions given in Eqs. (1) and (2). Note that C-S-H with different Ca/Si may also be considered just by modifying the amount of free portlandite (fraction A) present in the C-S-H.

When CO_2 is dissolved in brine, carbonic acid (H_2CO_3) is formed, which is subsequently dissociated into bicarbonate (HCO_3^-) and carbonate (CO_3^{2-}) ions. This process is summarized in two reactions (Eqs. (3) and (4)), where the intermediate formation of H_2CO_3 is omitted since its concentration is usually negligible. Consequently, the molar fraction of each species in relation to the total moles of carbon species depends on the pH of the solution, through the self-ionization reaction of water (Eq. (5)), as it can be appreciated in Fig. 2 which is discussed in Section 2.2.4.

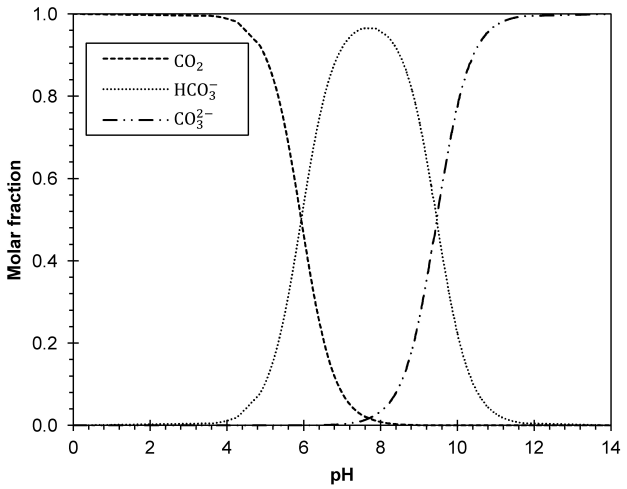

Fig. 2. Modelling result of carbon speciation as a function of pH in 0.5M NaCl brine at 50 °C.

The concentration gradient of aqueous carbon species causes a diffusion process from the brine towards the HCP, which is followed by a decrease of the pH of the pore solution in the HCP.

As pH lowers, the free portlandite in contact with the pore solution (zone II in Fig. 1) becomes unstable dissolving into Ca^{2+} (Reaction (1), towards right). While there is portlandite in contact with the pore solution, the pH will not lower below 9 (at 50 °C). At this pH the predominant species of aqueous carbon is CO_3^{2-} (Fig. 2), which will react with the Ca^{2+} resulting from portlandite dissolution forming calcite ($CaCO_3$), as it results from Reaction (6), towards left. Note that portlandite dissolution and calcite formations have opposite effects on the material porosity, which usually results in a slight increase of the capillary porosity. If carbon species continue entering, the free portlandite will eventually be exhausted. Consequently, the pH will decrease even further leading to the dissolution of the portlandite present

in the $CSH_{2.5}$ through Reaction (2), towards right, and slowing down but not stopping the formation of calcite (zone III in Fig. 1). In this zone, the volume balance between the dissolved portlandite (free and in $CSH_{2.5}$) and the formed calcite results in a net reduction of the material porosity. Additional ingress of carbon species will induce further reduction of the pH, driving calcite dissolution through Reaction (6), towards right, and continuing with the dissolution of the remaining portlandite in $CSH_{2.5}$ (zone IV in Fig. 1). Calcite is usually exhausted before portlandite in $CSH_{2.5}$, i.e. within zone IV. By losing calcium, $CSH_{2.5}$ becomes amorphous silicate hydrate ($SH_{1.5}$ in cement chemistry notation), which is assumed to be stable in contact with the carbonated brine. At this stage, HCP is completely degraded with practically no mechanical strength and with high permeability (zone V in Fig. 1). The calcium resulting from calcite and portlandite in $CSH_{2.5}$ dissolution raises locally the concentration of Ca^{2+} in the pore solution, enhancing its diffusive flux towards the brine, out of the HCP. The compounds forming the inert cement hydrates are considered to remain unaltered through the carbonation and dissolution processes. This is, of course, a major simplification. It is well known that aluminate and sulphate phases are only thermodynamically stable in highly alkaline waters (pH > 9) and, therefore, they are not stable in contact with carbonated brine. However, the effect of the dissolution/formation processes of the aluminate and sulphate phases does not seem to be determinant in the kinetics of the acid attack, accordingly with the numerical study performed by Huet et al. (2010). Moreover, other authors (Brunet et al., 2013; Fabbri et al., 2012; Raoof et al., 2012; Shen et al., 2013) have assumed the same simplification obtaining satisfactory results, as already mentioned in the Section 1.

$$Ca(OH)_{2\,(s)} \leftrightarrow Ca^{2+} + 2OH^- \tag{1}$$

$$[Ca(OH)_2][(SiO_2)(H_2O)_{1.5}] \leftrightarrow Ca^{2+} + 2\,OH^- + (SiO_2)(H_2O)_{1.5\,(s)} \tag{2}$$

$$CO_2(aq) + H_2O \leftrightarrow HCO_3^- + H^+ \tag{3}$$

$$HCO_3^- \leftrightarrow CO_3^{2-} + H^+ \tag{4}$$

$$H_2O \leftrightarrow H^+ + OH^- \tag{5}$$

$$CaCO_{3\,(s)} \leftrightarrow Ca^{2+} + CO_3^{2-} \tag{6}$$

All the processes described above are assumed to develop in a totally saturated environment, in which the water supply necessary for any of the mentioned reactions is assumed to be available at any time and any point of the material. This, in turn, also implies that the necessary water movements take place through the pore system. Under these conditions, the equations have been written without taking into account the water balance equation explicitly. At the same time, the water movements are assumed to be slow enough so that also advective terms do not need to be considered in the mass balance equations of solutes which are developed in the following. All these are, of course, simplifying assumptions that make the model more manageable and easier to implement. Comparison with available data may indicate whether these assumptions need to be revised in future developments.

2.2. Formulation

2.2.1. Solute mass balance

Assuming that the diffusion of aqueous species in the pore solution obeys Fick's diffusion law, averaging it in the saturated porous medium and posing the corresponding mass balance equation, the following diffusion-reaction equations for the continuum porous medium are obtained

$$\begin{cases} \dfrac{\partial(\phi c^{ca})}{\partial t} = \boldsymbol{\nabla}(D^{ca}\boldsymbol{\nabla}c^{ca}) + q^{ca} \\ \dfrac{\partial(\phi c^{tc})}{\partial t} = \boldsymbol{\nabla}(D^{tc}\boldsymbol{\nabla}c^{tc}) + q^{tc} \\ \dfrac{\partial(\phi c^{cl})}{\partial t} = \boldsymbol{\nabla}(D^{cl}\boldsymbol{\nabla}c^{cl}) \\ \dfrac{\partial(\phi c^{r})}{\partial t} = \boldsymbol{\nabla}(D^{r}\boldsymbol{\nabla}c^{r}) \end{cases} \tag{7}$$

where the superscripts ca, tc, cl and r indicate calcium, total carbon, chloride, and alkali (sodium and/or potassium), respectively; ϕ is the total porosity; c^β [mol/m^3] is the concentration of aqueous β-species in the pore solution expressed in moles per unit volume of pore solution; D^β [m^2/s] is the effective diffusivity of aqueous β-species in the porous medium (assumed isotropic), and q^β [mol/(m^3·s)] is the rate of production /consumption of β-species per unit volume of porous medium, which in turn is a function of the concentration of aqueous calcium and total carbon, i.e. $q^\beta = q^\beta(c^{ca}, c^{tc}, c^{cl}, c^r)$. Finally, $\boldsymbol{\nabla} = [\partial/\partial x \quad \partial/\partial y]^T$. The variable c^{tc} represents the summation of the molar concentrations of the different carbonic species in pore solution as it is given by Eq. (8), where the superscript $c0$ stands for CO_2, $c1$ for HCO_3^- and $c2$ for CO_3^{2-}.

$$c^{tc} = c^{c0} + c^{c1} + c^{c2} \tag{8}$$

Expressions of the production rate of calcium and total carbon are given in Eqs. (9) and (10) as functions of the net rates of production of solid species resulting from Reactions (1), (2) and (6), multiplied by the corresponding dimensionless stoichiometric coefficient (equal to 1 in all the considered reactions),

$$q^{ca} = -\phi\left(\Gamma^{CH} + \Gamma^{C\bar{C}} + \Gamma^{CSH}\right) \tag{9}$$

$$q^{tc} = -\phi\Gamma^{C\bar{C}} \tag{10}$$

In these expressions, Γ^α [mol/(m^3·s)] is the reaction rate of solid α-species per unit volume of pore solution (positive for solid formation, negative for solid dissolution) and the superscripts CH, $C\bar{C}$ and CSH indicate portlandite, calcite and $CSH_{2.5}$, respectively.

Note that chloride and alkalis are neither produced nor consumed in the HCP degradation process. However, they play and important role by modifying the pH and the ionic strength of the pore solution, as it is discussed below. The effect of other aqueous species (mainly species of Mg, Fe, Al, S and Si) usually present in cement pore solution has been neglected.

2.2.2. *Chemical kinetics*

The calculation of the sink/source terms q^β according to Eqs. (9) and (10) requires establishing the kinetic laws for Reactions (1), (2) and (6) in order to obtain the corresponding reaction rates Γ^α. To do so, it is assumed that the driving force of the dissolution/precipitation reaction of reactive solid α-species is $(\psi^\alpha - 1)$, where ψ^α is the dimensionless saturation index of the pore solution with respect to the solid α-species. Dissolution and precipitation reactions are assumed not to occur simultaneously but alternately depending on ψ^α. If $\psi^\alpha > 1$ the solution is over-saturated with respect to α-species and, consequently, the reaction progresses in the precipitation direction. If $\psi^\alpha < 1$, the solution is under-saturated and solid dissolution occurs. If $\psi^\alpha = 1$, the solid and the solution are in thermodynamical equilibrium. The resulting kinetic law is formulated for a generic solid α-species in Eq. (11), where k_f^α and k_d^α [mol/(m^3·s)] are

kinetic constants to be fitted and $\mathcal{N}^\alpha$ [mol/m³] is the molar concentration of the solid α-species

$$\Gamma^\alpha = \begin{cases} k_f^\alpha(\psi^\alpha - 1) & if\ \psi^\alpha \geq 1 \\ k_d^\alpha(\psi^\alpha - 1) & if\ \psi^\alpha < 1 \text{ and } \mathcal{N}^\alpha > 0 \\ 0 & if\ \psi^\alpha < 1 \text{ and } \mathcal{N}^\alpha = 0 \end{cases} \quad (11)$$

Strictly considered, the dissolution rate of the solid α -species should be proportional to the current surface area of the interface between the dissolving solid and the pore solution (Johannsen and Rademacher, 1999; Talman et al., 1990; Trapote-Barreira et al., 2014). Similarly, the formation rate of calcite depends on the type and area of the available seed surface (Zhang and Dawe, 1998). However, for the sake of simplicity, the interfacial surface area of each solid α-species is assumed to remain invariable and implicitly considered in the dissolution/formation kinetic constants. Although convenient for keeping the model simple, this 'first order' approach makes the kinetic constants dependent on the morphology of the solids in contact with the pore solution and, consequently, they need to be calibrated for each case analysed.

The saturation indexes considered for Reactions (1), (2) and (6) are defined as

$$\psi^{CH} = \frac{a^{ca} \cdot (a^{oh})^2}{K_{sp}^{CH}} \quad (12)$$

$$\psi^{C\bar{C}} = \frac{a^{ca} \cdot a^{c2}}{K_{sp}^{C\bar{C}}} \quad (13)$$

$$\psi^{CSH} = \frac{a^{ca} \cdot (a^{oh})^2}{K_{sp}^{CSH}} \quad (14)$$

where a^β is the thermodynamic activity of the aqueous β-species in pore solution, which is calculated as described in the next section; the superscript *oh* stands for OH^-; K_{sp}^α is the saturation product constant of the solid α-species dissolution. The saturation product constants for portlandite and calcite are readily obtained from thermodynamic databases as a function of temperature (e.g. from THERMODDEM(2014)). In the case of $CSH_{2.5}$, in contrast, K_{sp}^{CSH} needs to be fitted with experimental data at the considered temperature or, in the absence of that data, with results from a more sophisticated C-S-H solubility model. For this paper, K_{sp}^{CSH} has been estimated based on experimental measurements of equilibrium concentrations of calcium in water in contact with C-S-H at different temperatures, summarized from different sources by Gisby and Davies (2007). See Table 1 for the adopted K_{sp}^α values at 20 and 50 °C.

Table 1
Saturation product constants and equilibrium constants at 20 and 50 °C, given for activities in [mol/L]. Notes: (a) from THERMODDEM (2014); (b) from Lide (2004, pp. 8–86); (c) estimated value.

	20 °C	50 °C	Notes
Saturation product constants			
K_{sp}^{CH}	7.515E-06	3.236E-06	(a)
$K_{sp}^{C\bar{C}}$	3.554E-09	2.007E-09	(a)
K_{sp}^{CSH}	7.562E-09	3.236E-09	(c)
Equilibrium constants			
k_{eq}^{c0}	4.136E-07	5.171E-07	(a)
k_{eq}^{c1}	4.246E-11	6.748E-11	(a)
k_{eq}^{w}	6.893E-15	5.352E-14	(b)

Although amorphous silica hydrate ($SH_{1.5}$) results from the loss of calcium of $CSH_{2.5}$, from the numerical point of view this process is treated as dissolution of $CSH_{2.5}$ with simultaneous formation of $SH_{1.5}$ at the same pace, i.e.

$$\Gamma^{SH} = -\Gamma^{CSH} \quad (15)$$

Note that the inverse reaction, i.e. the formation of $CSH_{2.5}$ by incorporating calcium to $SH_{1.5}$ is not allowed. Furthermore, since aqueous silicate species are not considered in the formulation, the dissolution of $SH_{1.5}$ is not allowed either.

Finally, the mass balance equation of solid α-species is given by

$$\frac{\partial(\mathcal{N}^\alpha \mathcal{U})}{\partial t} = \phi \mathcal{U} \Gamma^\alpha \quad (16)$$

where $\mathcal{U}$ [m³] is the total volume of porous medium, $\mathcal{N}^\alpha \mathcal{U}$ is the total quantity of (the total number of moles of) solid α-species and $\phi\mathcal{U}$ is the volume of pore solution. Since no significant change in the total volume due to carbonation is expected, the time derivative of $\mathcal{U}$ can be neglected.

2.2.3. Thermodynamic activity

In order to account for deviations from ideal behaviour of the aqueous β-species in pore solution which are due to the interaction with other species, activity a^β is considered in chemical equilibrium equations instead of concentration c^β. Activity and concentration are related by means of a dimensionless factor γ^β (activity coefficient) as follows

$$a^\beta = \gamma^\beta c^\beta \quad (17)$$

In the present formulation, activity coefficients are calculated using Eq. (18), where z^β is the number of electric charges of the β-species considered, I [mol/L] is the ionic strength of the solution and A_γ is the Debye-Hückel parameter. Equation (18) is the well-known Davies Equation with the modification of the second term proposed by Samson and Lemaire (1999), in order to extend its applicability to solutions at ionic strengths up to 1.20 mol/L. The expression of I is given in Eq. (19). The Debye-Hückel parameter A_γ is calculated as a function of temperature with the approximated expression proposed by Pitzer (1991, p. 297). Values of A_γ at 20 and 50 °C are 0.506 and 0.535, respectively. The effect of pressure on A_γ has been neglected.

$$log_{10}(\gamma^\beta) = -A_\gamma \cdot (z^\beta)^2 \cdot \left[\frac{\sqrt{I}}{1+\sqrt{I}} - \left(0.2I - \frac{1}{24}I^2\right)\right] \quad (18)$$

$$I = \frac{1}{2}\sum_\beta c^\beta \cdot (z^\beta)^2 \quad (19)$$

2.2.4. Chemical speciation

The chemical equilibrium equations corresponding to Reactions (3) to (5), are given in Eqs. (20) to (22), where k_{eq}^{c0}, k_{eq}^{c1} and k_{eq}^{w} are equilibrium constants dependent on temperature (Table 1), and the superscripts h and w stand for H^+ and H_2O, respectively. Additionally, the electric charge balance equation of the pore solution (Eq. (23)) must be fulfilled.

$$k_{eq}^{c0} = \frac{a^h \cdot a^{c1}}{a^{c0}} \quad (20)$$

$$k_{eq}^{c1} = \frac{a^h \cdot a^{c2}}{a^{c1}} \quad (21)$$

$$k_{eq}^{w} = a^h \cdot a^{oh} \quad (22)$$

$$\sum_\beta z^\beta c^\beta = 0 \quad (23)$$

Considering these equations plus Eqs. (8), (17) and (18), it is possible to determine equilibrium concentrations of secondary species ($c^{c0}, c^{c1}, c^{c2}, c^{oh}, c^{h}$) as a function of the concentrations of the primary ones ($c^{ca}, c^{tc}, c^{r}, c^{cl}$) by solving the resultant non-linear system of equations. This is achieved by a mix of analytical and numerical procedures. First, a unique polynomial equation of fourth order in terms of c^h has been obtained by assuming constant values for activity coefficients, i.e. ignoring Eq. (18), and operating with the rest of the equations. Then, trial values of the activity coefficients are adopted and the polynomial equation is solved numerically by means of the bisection method. To do so, the sought roots is bracketed by assuming two extreme sceneries, one acidic, with $c^{ca} = 0$, and the other basic, with $c^{tc} = 0$. Once the value c^h is known, the rest of the secondary species concentrations are readily obtained, and the corresponding, new, activity coefficients are calculated with Eq. (18). If the new activity coefficients differ less than 0.001 from the initially adopted ones, the calculation concludes. Otherwise, the procedure is repeated until convergence is reached.

In order to illustrate the capabilities of the speciation formulation proposed, some modelling results are presented. In Fig. 3a, pH is plotted as a function of calcium and total carbon concentrations in 0.5M NaCl brine at 50 °C. It can be seen that pH increases with increasing c^{ca} and decreases with increasing c^{tc}. In Fig. 3b to d, saturation indexes are plotted in the same conditions. The thicker solid lines ($\psi^\alpha = 1$) indicate the limit between the dissolution and precipitation zones. In Fig. 2, the associated carbon speciation is plotted as a function of pH. It shall be noted that CO_3^{2-}, needed for calcite formation, is the predominant carbon species only for pH > 10.

2.2.5. Volumetric fractions balance

The total volume of porous medium $\mathcal{U}$ [m³] is given by

$$\mathcal{U} = \mathcal{U}^{cp} + \sum_\alpha \mathcal{U}^\alpha \tag{24}$$

where $\mathcal{U}^\alpha$[m³] is the volume of solid α-species, and $\mathcal{U}^{cp}$[m³] is the capillary porosity, i.e. the part of the material volume that is not occupied by the solid phases and which is assumed to be filled with free water.

The volume of the α-species is obtained as a function of its molar concentration with

$$\mathcal{U}^\alpha = \omega^\alpha \mathcal{N}^\alpha \mathcal{U}\,; \quad \omega^\alpha = \eta^\alpha/(1-\phi^\alpha) \tag{25}$$

where ω^α[m³/mol] is the apparent molar volume, η^α[m³/mol] is the specific molar volume, and ϕ^α is the intrinsic porosity of the solid α-species. Intrinsic porosity is defined as the ratio between gel water volume and total apparent volume of phase α. 'The gel water', in contrast with capillary water, 'is visualised as being within the influence of absorbing forces' (Brouwers, 2004). Note that for crystalline solids such as portlandite and calcite the intrinsic porosity is null ($\phi^{CH} = \phi^{C\bar{C}} = 0$).

Since the HCP is assumed to be fully saturated with water, the total volume of pore solution $\mathcal{U}^{ps}$, which includes free and gel water, is equal to the total volume of pores, i.e.

$$\mathcal{U}^{ps} = \mathcal{U}^{cp} + \sum_\alpha \phi^\alpha \mathcal{U}^\alpha \tag{26}$$

Finally, capillary porosity ϕ^{cp} and total porosity ϕ are given by

$$\phi^{cp} = \frac{\mathcal{U}^{cp}}{\mathcal{U}} \quad \text{and} \quad \phi = \frac{\mathcal{U}^{ps}}{\mathcal{U}} \tag{27}$$

2.2.6. Effective diffusion coefficients

The effective diffusivity of β-species (D^β) in water-saturated HCP depends on the characteristics of its microstructure (capillary porosity, gel porosity, tortuosity, connectivity, etc.). As

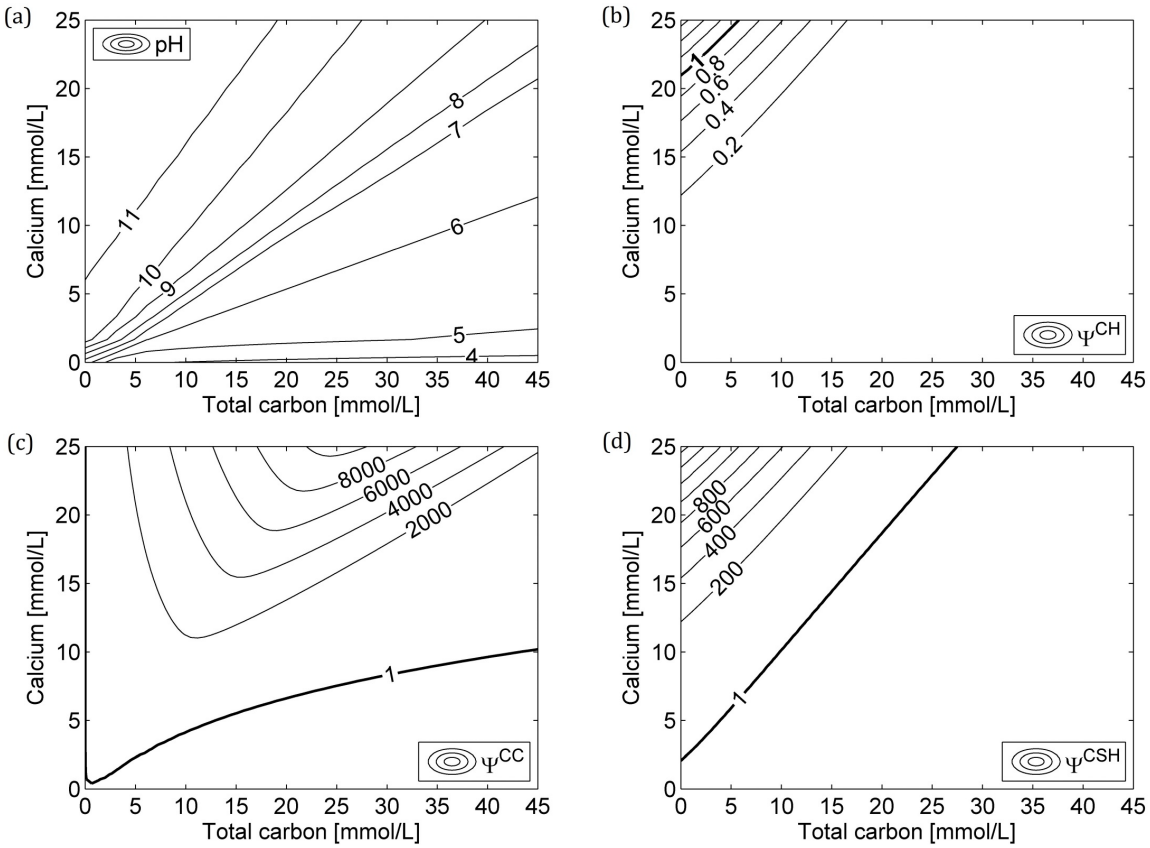

Fig. 3. Saturation indexes and pH as functions of calcium and total carbon concentrations in 0.5M NaCl brine at 50 °C: (a) pH; (b) portlandite saturation index; (c) calcite saturation index; (d) $CSH_{2.5}$ saturation index.

the carbonation-dissolution front advances, the microstructure of the HCP is deeply altered and, consequently, its effective diffusivity is expected to suffer significant variations. In order to asses these variations, the effective diffusivity of the β-species in the HCP (D^β) is calculated by means of the analytical formula proposed by Oh and Jang (2004) and given in Eqs. (28), where D_0^β [m²/s] is the diffusivity of the β-species in bulk water, i.e. in a free, infinitely diluted solution. This equation uses four dimensionless parameters which characterize the microstructure of the HCP, namely the capillary porosity (ϕ^{cp}), the percolation threshold (ϕ_c), the normalized diffusivity of the solid phase (D_s^β/D_0^β), and the percolation exponent (n). By fitting experimental measurements of chloride diffusivity in a number of HCP specimens with and without mineral admixtures, Oh and Jang found that there exist some constant values of n and D_s^β/D_0^β for each type of cement paste, and that realistic values for HCP without mineral admixtures are $n \approx 2.7$ and D_s^β/D_0^β ranging between 5×10^{-5} and 1×10^{-3}. The percolation threshold was found to be $\phi_c \approx 0.17-0.18$ in all cases. In the context of the decalcification of the HCP these parameters are expected to be altered. In particular, the percolation exponent n which is representative of the tortuosity of the pore structure is expected to be reduced as the C-S-H is dissolved. In order to introduce this effect, the percolation exponent will be updated with Eq. (29), where n_i and n_f are the percolation exponent for unaltered and for completely decalcified HCP, respectively, and $\mathcal{U}_i^{CSH}$ is the volume of $CSH_{2.5}$ in the unaltered HCP. In this way, the effective diffusivity is related with the evolution of the solid fractions through Eqs. (27) and (29).

$$\frac{D^\beta}{D_0^\beta} = \left(m_\phi + \sqrt{m_\phi^2 + \frac{\phi_c}{1-\phi_c}\left(\frac{D_s^\beta}{D_0^\beta}\right)^{1/n}} \right)^n \tag{28a}$$

$$m_\phi = \frac{1}{2}\left[\left(\frac{D_s^\beta}{D_0^\beta}\right)^{1/n} + \frac{\phi^{cp}}{1-\phi_c}\left(1-\left(\frac{D_s^\beta}{D_0^\beta}\right)^{1/n}\right) - \frac{\phi_c}{1-\phi_c} \right] \tag{28b}$$

$$n(t) = n_i - (n_i - n_f)\left(1 - \frac{\mathcal{U}^{CSH}(t)}{\mathcal{U}_i^{CSH}}\right) \tag{29}$$

Although Oh and Jang have only validated their formula with diffusion tests at 25 °C, its applicability will be extended for 20 and 50 °C. These extrapolations are based on the results of Samson and Marchand (2007), who found that the ratio D^β/D_0^β remains almost constant for temperatures between 4 to 40 °C, indicating that an increase in temperature only contributes to increase the thermal agitation of ions in solution without affecting the microstructure of the HCP.

The diffusion coefficients of the β-species in bulk water at standard conditions (25 °C, 0.1 MPa) can be easily found in physics handbooks (e.g. in Lide (2004)). These coefficients can be extrapolated to other conditions by means of the Stokes-Einstein relation given in Eq. (30), where μ_0 [Pa·s] is the viscosity of the bulk aqueous medium and T [°K] is the absolute temperature (Yuan-Hui and Gregory, 1974). The diffusion coefficients in bulk water at standard conditions for the aqueous species considered in the model are given in Table 2, as well as the diffusion coefficients in bulk water at 20 and 50 °C calculated using Eq. (30) with water viscosities obtained from Kestin et al. (1981). Since in Eq. (7) the diffusion of the three carbonic species is modelled by means of unique field variable (c^{tc}), a representative diffusion coefficient D_0^{tc} needs to be adopted. It has been found by fitting experimental results from the literature (see Section 3) that the diffusion coefficient to be used for the total carbon field shall be close to the one of $CO_{2(aq)}$, i.e. $D_0^{tc} \approx D_0^{c0}$.

$$\left(\frac{D_0^\beta \mu_0}{T}\right)_{T1} = \left(\frac{D_0^\beta \mu_0}{T}\right)_{T2} \tag{30}$$

Table 2
Diffusion coefficients in [10^{-9} m²/s] for aqueous species in bulk water at different temperatures. Diffusivities in bulk water at 25 °C are from Lide (2004, pp. 6-222–95). Diffusivities in bulk water at 20 and 50 °C have been extrapolated using Stoke-Einstein relation with water viscosities given in Kestin et al. (1981).

Species	Symbol	20 °C	25 °C	50 °C
$CO_{2(aq)}$	$D_0^{c0} \approx D_0^{tc}$	1.668	1.910	3.368
HCO_3^-	D_0^{c1}	1.035	1.185	2.090
CO_3^{2-}	D_0^{c2}	0.806	0.923	1.628
Ca^{2+}	D_0^{ca}	0.692	0.792	1.397
Cl^-	D_0^{cl}	1.775	2.032	3.583
Na^+	D_0^r	1.165	1.334	2.352
K^+	D_0^r	1.709	1.957	3.451

2.3. Numerical implementation

The above-described formulation has been implemented in the Finite Element code DRACFLOW, in-house developed by the group of Mechanics of Materials at UPC (MECMAT). This code has been previously used to model a number of durability problems in concrete such as drying shrinkage (Idiart et al., 2011a), external sulphate attack (Idiart et al., 2011b), Alkali-Silica Reaction (Liaudat et al., 2016) and high temperature (Rodriguez et al., 2017).

The spatial discretization of Eq. (7) by the Finite Element Method, results in the following matrix equation for a given boundary value problem:

$$\boldsymbol{E}\boldsymbol{c} + \boldsymbol{S}\dot{\boldsymbol{c}} - \boldsymbol{Q} = \boldsymbol{0} \tag{31}$$

where $\boldsymbol{E}$ [m³/s] is the effective diffusivity matrix, $\boldsymbol{S}$ [m³] is the capacity matrix, $\boldsymbol{Q}$ [mol/s] is the sink/source vector, and $\boldsymbol{c}$[mol/m³] and $\dot{\boldsymbol{c}}$ [mol/(m³·s)] are the nodal concentration and nodal concentration rate vectors, respectively. If the problem is to be solved between an initial time t_0 and a final time t_f, a partition of the time interval $[t_0, t_f]$ is considered, which results in a series of time increments $\Delta t_{n+1} = t_{n+1} - t_n$. In each time step, the mass balance must be guaranteed, i.e.

$$\mathbb{I}_{n+1} = \int_0^{\Delta t_{n+1}} [\boldsymbol{E}(\tau)\boldsymbol{c}(\tau) + \boldsymbol{S}(\tau)\dot{\boldsymbol{c}}(\tau)]\, d\tau - \int_0^{\Delta t_{n+1}} \boldsymbol{Q}(\tau)\, d\tau = \boldsymbol{0} \tag{32}$$

where $\tau = t - t_n$ with $0 \le t \le t_{n+1}$. By discretizing in time this integral equation, assuming linear variation of $\boldsymbol{c}(\tau)$ in Δt_{n+1} between $\boldsymbol{c}_n = \boldsymbol{c}(t_n)$ and $\boldsymbol{c}_{n+1} = \boldsymbol{c}(t_{n+1})$, the numerical problem is reduced to find the vector $\boldsymbol{c}_{n+1}$ that minimizes vector $\mathbb{I}_{n+1}$, what is done by means of a Newton-Raphson numerical procedure. The first integral in Eq. (32) is discretized by means of the generalized trapezoidal rule with a weighting factor θ, that in this paper has been taken as $\theta = 1$ (Backward Euler scheme). The second integral, due to the abrupt changes in chemical rates, requires a more accurate integration. Instead of considering a linear variation of $\boldsymbol{Q}$ in Δt_{n+1}, the second integral is obtained by assuming that concentrations vary linearly in Δt_{n+1}, subdividing the time step Δt_{n+1} in a number sub-steps and calculating the reaction rates Γ^α during each sub-step with the concentrations at the mid-time of the sub-step. With these simplifications, the integral is then solved for each sub-step analytically.

3. Modelling results

In order to validate the proposed formulation, part of the experiments performed by Duguid and Scherer (2010) of well cement degradation due to exposure to carbonated brine have been simulated.

3.1. The experiments

The experiments consisted of cylindrical neat cement paste samples in a reactor that had a continuous flow of carbonated 0.5 M NaCl brine pumped from the inlet at the bottom of the reactor to the outlet at the top. The experiments were performed for two different temperatures (20 and 50 °C) and two different pH of the carbonated brine solution at room temperature (pH 2.4 and pH 3.7), in order to study the sensitivity of the degradation process to these parameters. The solution with pH 3.7 was obtained by saturating the 0.5 M NaCl with CO_2 at room temperature. In contrast, the solution with pH 2.4 was obtained by adding HCl to the solution with pH 3.7. The concentration of CO_2 and HCl needed to reach the prescribed pH were not specified. The cement paste samples were made with class H cement (API Spec. 10A, 2002) and water/cement ratio of 0.38, using cylindrical moulds of 7.5 mm diameter and 200 mm length. Once demoulded, the samples were placed in 0.5 M NaCl solution to cure at either 20 or 50 °C for 12 months, previously to their exposure to carbonated brine. After curing, total porosity and apparent density were measured, being 47 % and 1.95 g/cm^3 for samples cured at 20 °C, and 48 % and 1.80 g/cm^3 and for samples cured at 50 °C. Evolution of the degradation front was followed by cutting small samples from the cement cylinder in the reactor at different times throughout the experiment. On these samples, visual measurements of depth of advance of different fronts were performed.

3.2. Modelling conditions

The cylindrical samples have been simulated as a 1D axisymmetric problem, i.e. only radial diffusion in the sample is considered. This simplification is justified by the high aspect ratio (length/ diameter) of the samples. The sample radius of 3.75 mm was discretized with 50 equal size linear finite elements. All simulations were performed for a total time of 720 hours (30 days) discretized in increments of 0.2 hours.

Prescribed normal diffusion fluxes j^β [mol/(m^2·s)] (Neumann boundary conditions) were imposed at the outer end ($\partial\Omega$), accordingly with Eq. (33), where c_e^β is the concentration of the aqueous β-species in the carbonated brine surrounding the specimen and $\hbar$ [m/s] is the 'convection' coefficient, which is assumed to be the same for all the aqueous species considered and to remain constant during the tests. The value of $\hbar$ adopted for all the performed simulations was 0.006 m/h. In the experimental setup the carbonated brine in the reactor is continuously renewed in order to keep the exposure conditions as constant as possible. However, measurements of pH and calcium concentration of the effluent during the tests did show some variations. The introduction of these variations in preliminary simulations did not induce significant changes in the results. Consequently, for the sake of simplicity, the prescribed values of c_e^β are also assumed to remain constant during the test.

$$j^\beta = \hbar\left(c^\beta - c_e^\beta\right) \text{ on } \partial\Omega \tag{33}$$

Since the concentration of CO_2 and HCl in the carbonated brine has not been informed, it has been necessary to estimate them by simulating the procedure followed by Duguid and Scherer. To do so, we have considered 0.5 M NaCl solution bath at room temperature (assumed to be 20 °C), in which CO_2 was added until the prescribed pH 3.7 was reached. This results in total carbon concentration of 46 mmol/L, which is close to the CO_2 solubility in 0.5 M NaCl at 20 °C and 1 bar, according to the CO_2 solubility model of Duan and Sun (2003). Then, keeping this total carbon concentration constant, the concentration of chloride is raised until the prescribed pH 2.4 is reached, which occurred for a chloride concentration of 504 mmol/L. Since Duguid and Scherer have not given any explicit or implicit information about the carbonated brine composition at 50 °C and it is also unclear what the gas pressure was during tests, we additionally assumed that the estimated concentrations of total carbon and chloride in the carbonated brine will be the same at both tests temperatures. The estimated composition of the carbonated brine used in each test is summarized in Table 3.

Table 3
Test identification and exposure conditions.

Test Id.	Temp. °C	pH at 20 °C	c^{cl} mmol/L	c^{ca} mmol/L	c^r mmol/L	c^{tc} mmol/L
A	50	2.4	504	0	500	46
B	20					
C	50	3.7	500			
D	20					

The long-time exposure to 0.5 M NaCl brine during the curing stage, makes it possible to assume that, at the beginning of the exposure to the carbonated brine, concentration of alkali (sodium) and chloride was homogeneous in the sample and equal to that of the brine, i.e. $c^r = 500$ mmol/L and $c^{cl} = 500$ mmol/L. The initial calcium concentration is given by the equilibrium concentration of portlandite in contact with 0.5 M NaCl brine at 20 °C ($c^{ca} = 26.69$ mmol/L) and 50 °C ($c^{ca} = 20.95$ mmol/L).

The determination of the initial concentration of solid compounds to be used in the simulations has been done in two steps. The first step consisted in estimating the initial amount of cement hydration products in the cement paste samples using the expressions given by Brouwers (2005, 2004), which are based on the work of Powers and Brownyard (1946). By introducing the (nonhydrated) cement composition and the w/c ratio of the paste, these expressions allow us to estimate the amount of the different cement hydration products as well as the different porosity fractions (gel and capillary porosity). Since cement composition have not been given by Duguid and Scherer, the following typical mineralogical composition of API class H cement (SPE, 2016) has been adopted: 50 wt% C_3S, 30 wt% C_2S, 5 wt% C_3A, 12 wt% C_4AF and 3 wt% of others (free CaO, MgO, etc.). The formulae proposed by Brouwers were only fitted with cement pastes cured at room temperature, so they are not strictly applicable to the cement paste samples cured at 50 °C. Furthermore, significant changes in microstructures are expected when increasing curing temperature. In particular, as the curing temperature increases, the amount of gel water in the C-S-H decreases, which in turn determines an increase in the C-S-H density and, consequently, also in the capillary porosity of the HCP (Gallucci et al., 2013). In the absence of better data, the applicability of Brouwers' expressions has been extended to HCP cured at 50 °C by increasing the density of the $C_{1.7}SH_{3.2}$ and reducing the amount of gel water given by Brouwers in proportion similar to the observed by Gallucci et al. (2013).

The resulting compositions obtained for the specimens cured at 20 and 50 °C are summarized in Table 4, as well as the volume fractions of capillary pores. The maturity factor (degree of hydration) was assumed to be 0.90. It has been necessary to add an additional volume of voids to the volume fractions given by Brouwers' expressions in order to reach the total porosities and apparent densities measured by Duguid and Scherer. This may indicate that some air has been trapped in the samples in the casting process. (The alternative possibility was also explored of considering a lower maturity factor that, according to Brouwers'

formulae, would lead to the observed porosities; however, this yielded very low maturity factors in the order of 0.35, clearly unrealistic for samples cured in water for a period of 1 year). The densities and porosity corresponding with the calculated composition were 1.96 and 0.47 for the 20 °C samples and 1.88 and 0.48 for the 50 °C samples, which are in good agreement with the values informed by Duguid and Scherer (and also reproduced in Section 3.1).

Recent experimental investigations performed by Muller et al. (2013; 2013) has demonstrated than the assumption of the model of Powers and Brownyard (and consequently that of the Brouwers' formulae) of a constant bulk density for the formed C-S-H may be not accurate. Muller's results indicate that bulk C-S-H (solid + gel water) progressively densifies as the cement hydration progresses. Although, this may lead to non-negligible differences in the predicted capillary/gel porosity at early age, it has been explicitly noted by Muller at al. (2013) that the model by Powers and Brownyard still produces good results for later ages (larger degrees of hydration) as the ones considered in this paper.

In a second step, the compositions in Table 4 were recalculated in terms of the solid compounds considered in the model and presented in Table 5. The $C_{1.7}SH_{3.2}$ has been split in $CSH_{2.5}$ and CH, as explained in Section 2.1. The molar volume of $CSH_{2.5}$ was calculated by subtracting the volume of the split CH and assuming that the volume of gel water per mole of C-S-H is the same for $C_{1.7}SH_{3.2}$ as for $CSH_{2.5}$. The volumes of $C_6AFS_2H_8$, C_4AH_{22} and 'others' have been grouped in the 'Inert CP' component. The number of moles of Inert CP is obtained by assigning a fictitious value of molar volume. The gel porosity is assumed to be the same in the $CSH_{2.5}$, the inert CP, and the $SH_{1.5}$, with a value adopted in order to obtain the same total volume of gel pores calculated according with Brouwers' formulae.

Table 4
Estimated composition of hydrated cement pastes cured at 20 and 50 °C used in the experiments by Duguid and Scherer (2010). Values corresponding to 50 °C in brackets. Molar volumes at 20 °C from Brouwers (2005).

	$\mathcal{N}^\alpha$	ω^α	$\mathcal{U}^\alpha$
	10^3 mol/m^3	10^{-6} m^3/mol	m^3/m^3
$C_{1.7}SH_{3.2}$	3.728 (3.640)	94.58 (81.45)	0.353 (0.296)
CH	4.028 (3.933)	33.05 (33.05)	0.133 (0.130)
$C_6AFS_2H_8$	0.268 (0.261)	285.02 (285.02)	0.076 (0.075)
C_4AH_{22}	0.201 (0.196)	419.45 (419.45)	0.084 (0.082)
Other solids	N.A.	N.A.	0.098 (0.064)
Cap. Pores	N.A.	N.A.	0.100 (0.177)
Other voids	N.A.	N.A.	0.157 (0.176)
		SUM	1.000 (1.000)

Table 5
Initial concentration and volumetric parameters of the solid compounds considered in the model for cement paste cured at 20 and 50 °C. Values corresponding to 50 °C in brackets.

	$\mathcal{N}^\alpha$	ω^α	ϕ^α	$\mathcal{U}^\alpha$
	10^3 mol/m^3	10^{-6} m^3/mol	m^3/m^3	m^3/m^3
$CSH_{2.5}$	3.73 (3.64)	71.4 (58.3)	0.406 (0.290)	0.266 (0.212)
CH	6.64 (6.48)	33.1 (33.1)	0.000 (0.000)	0.219 (0.214)
Inert CP	2.58 (2.20)	100.0 (100.0)	0.406 (0.290)	0.258 (0.220)
$C\bar{C}$	0.00 (0.00)	36.9 (36.9)	0.000 (0.000)	0.000 (0.000)
$SH_{1.5}$	0.00 (0.00)	52.6 (50.4)	0.406 (0.290)	0.000 (0.000)
Cap. Pores	N.A.	N.A.	1.000 (1.000)	0.256 (0.353)
			SUM	1.000 (1.000)

For the calculation of effective diffusivity (Section 2.2.5) the following parameter values have been chosen to fit the experimental results: $n_i = 2.7$, $n_f = 0.1, \phi_c = 0.18$, $D_s^\beta/D_0^\beta = 1\times10^{-3}$ for specimens cured at 20 °C and $D_s^\beta/D_0^\beta = 1\times10^{-4}$ for specimens cured at 50 °C. Lower diffusivity in the solid phase D_s^β is expected in cement pastes cured at higher temperatures due to the reduction of gel porosity reported by Gallucci et al. (2013). However, the effective diffusivity in the specimens cured at 50 °C is higher than that of those cured at 20 °C, since the effect of the increased capillary porosity is determinant. Diffusivities of calcium and carbon aqueous species in bulk brine at 20 and 50 °C are the ones given in Table 2. For the total carbon variable, it has been assumed that $D_0^{tc} = D_0^{c0}$. The adopted diffusivity for alkalis (D_0^r) is irrelevant for these cases, as it is discussed in Section 3.3.

Finally, the saturation product constants (K_{sp}^α) and the equilibrium constants (k_{eq}^α) used in the simulations are the ones given in Table 1, and the dissolution kinetic constants chosen to fit the experimental results are given in Table 6. The kinetic constants were found not no vary significantly with temperature and, therefore, the same values were used for tests at 20 and 50 °C. Formation kinetic constant of portlandite has not been fitted since the correspondent saturation index remains well under 1 in all the simulations. As stated in Section 2.2.2, $CSH_{2.5}$ formation was not allowed.

Table 6
Kinetic constants used in simulations given in [mol/(m³·h)].

k_d^{CH}	$k_d^{C\bar{C}}$	k_d^{CSH}	$k_f^{C\bar{C}}$
1.000E+02	5.000E+02	2.000E+01	5.000E-02

3.3. Calibration procedure

In this section, the calibration procedure followed to obtain the unknown model parameters is summarized. This calibration procedure comprised two steps. The first step consisted in independently estimating:

- The saturation product of $CSH_{2.5}$ (K_{sp}^{CSH}) at 20 and 50 °C by comparing with experimental results from the literature as explained in Section 2.2.2.
- The total carbon and chloride concentrations (c^{tc}, c^{cl}) in the carbonated brines used in the experiments by fitting the measured values of pH, as explained in Section 3.2.
- The initial volume fractions in cement samples ($\mathcal{U}^\alpha$) and the corresponding total (ϕ) and capillary (ϕ^{cp}) porosities by fitting the measured densities and total porosities, as explained in Section 3.2.

In the second step, the following parameters were calibrated simultaneously by fitting the experimental results of Tests C (pH 3.7, 50 °C) and D (pH 3.7, 20 °C):

- 'Convection' coefficient: $\mathcal{k}$
- Diffusion parameters: $n_i, n_f, D_s^\beta/D_0^\beta$
- Kinetics constants: $k_f^{C\bar{C}}, k_d^{CSH}, k_d^{C\bar{C}}, k_d^{CH}$

As part of this second step, preliminary sensitive analyses (not presented here) were performed for each calibrated parameter in order to guide the calibration process.

The experimental results of Tests A and B were then predicted with the model using the same parameter values, leading to satisfactory fitting as discussed in the following Section 3.4.

3.4. Results and discussion

In Fig. 4, calculated radial profiles of total carbon, calcium and chloride concentrations in pore solution, as well as the corresponding pH, are plotted at different test times for Test A (pH 2.4 at 50 °C). Since alkalis are neither produced nor consumed by the considered reactions and since the initial concentration is the same in the brine and in the pore solution, the alkalis concentration remains constant at 500 mmol/L during the test.

The sigmoid form of the total carbon profiles is due to the combined effect of, on one hand, the consumption/production of aqueous carbon associated with the formation/dissolution of calcite and, on the other hand, the increase of the effective diffusivity on the degraded zones. In the 25d and 30d profiles the total carbon concentration rises slightly over the boundary concentration due to the combined effect of calcite dissolution and the rise of total carbon concentration at the symmetry axis of the specimen.

Due to its relative high diffusivity and the absence sink terms, chloride concentration rapidly reaches equilibrium with the concentration at the boundary.

Initial calcium content in the specimen corresponds to the saturation concentration for portlandite dissolution in 0.5 M NaCl brine at 50 °C. Firstly, the rapid ingress of chloride lowers the pH in the unaltered zone driving dissolution of portlandite until the new calcium equilibrium concentration is reached. While there is still some portlandite to be dissolved the calcium concentration remains over 20 mmol/L, but once portlandite content is exhausted the calcium concentration reduces steadily towards the boundary of the specimen, with the exception of local peaks due to the formation of calcite and subsequent dissolution of $CSH_{2.5}$, as it is explained below.

Note that the imposed boundary condition (Eq. (33)) implies that the concetrations at the boundary are not constant but steadily progress towards the concentrations in the carbonated brine (c_e^{β}).

The pH profiles are determined mainly by the total carbon and calcium profiles, changing from over 11.5 at the unaltered zone to less than 5 at the specimen boundary, with a sharp drop coinciding with the portlandite exhaustion.

The evolution of the six volumetric fractions with time at a depth of 1.50 mm is plotted in Fig. 5. There, the progressive decalcification of the material through the dissolution of portlandite and $CSH_{2.5}$ until only amorphous silica remains is clearly appreciated. The precipitation of calcite momentarily reduces the material porosity, but later on it is substantially increased.

In Fig. 6, calculated radial profiles of different model variables for Test A (pH 2.4 and 50 °C) after 15 days of exposure are plotted together in order to make apparent the existent relationships between them. In Fig. 6a changing volumetric fractions and total carbon effective diffusivity are plotted together. Fig. 6b presents the radial profiles of the different carbon species. Finally, in Fig. 6c saturation indexes and pH profiles are plotted together.

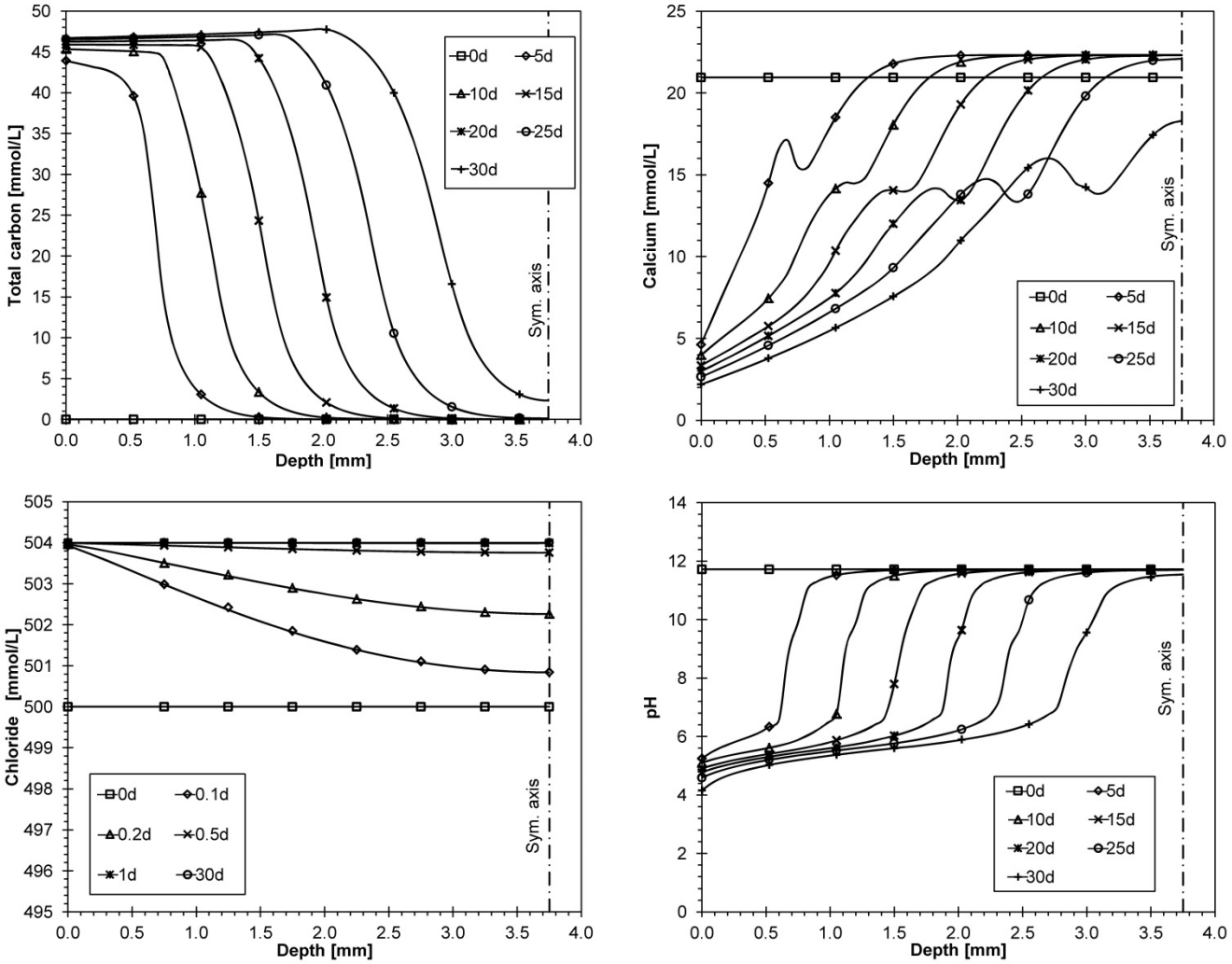

Fig. 4. Calculated radial profiles at different times of total carbon, calcium and chloride concentration in pore solution, as well as the corresponding pH, for Test A (50 °C and pH 2.4).

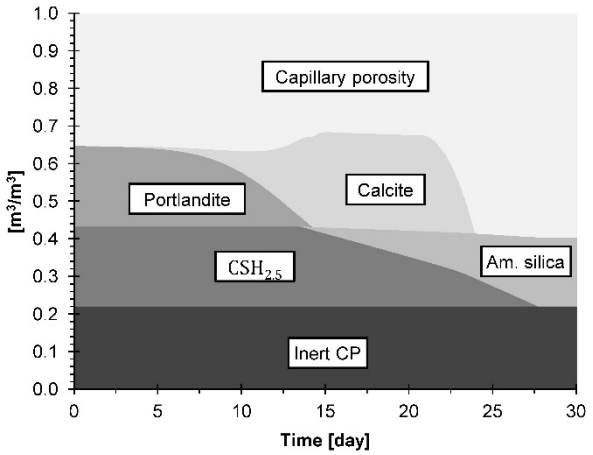

Fig. 5. Time evolution of volumetric fractions at a depth of 1.50 mm for Test A (50 °C and pH 2.4).

In these profiles, the five characteristic zones described in Section 2.1 can be distinguished. The first one (I) corresponds to the unaltered material in the interior of the specimen. Even though some carbon has reached this zone, the amount is so low that no significant alteration of the material is perceived.

In the second zone (II) the carbon concentration is higher driving the dissolution of portlandite and a consequent increase of calcium concentration in the pore solution. Note that portlandite acts as a pH buffer keeping it well above 10. In this pH range the preponderant carbon species is CO_3^{2-}, allowing the formation of calcite. The simultaneous dissolution of portlandite and formation of calcite has the net effect of a slight reduction of the material porosity and, consequently, of the material effective diffusivity.

The third zone (III) is marked by a sharp drop of the pore solution pH due to an even higher concentration of carbon and the exhaustion of portlandite. As the pH decreases, the $CSH_{2.5}$ saturation index decreases, eventually going bellow 1 at pH close to 10, triggering its dissolution. Similarly, the calcite saturation index decreases several orders resulting in a practically null rate of formation. Note that additional calcite is only formed while the pH remains over 8, since below 8 there is practically no CO_3^{2-} in pore solution. The combination of the production of calcium due to $CSH_{2.5}$ dissolution with the end of aqueous calcium consumption to form calcite results in a local peak of aqueous calcium concentration that is appreciated in Fig. 4.

The calcium produced by $CSH_{2.5}$ dissolution allows the formation of some additional calcite only while the pH remains over 8, since bellow 8 there is practically no CO_3^{2-} in pore solution. The volume balance in this zone between calcite formation and $CSH_{2.5}$ dissolution causes an additional reduction of the porosity, which in this zone reaches its minimum.

The fourth zone (IV) is marked by an additional reduction of the pH which takes the calcite saturation index below 1, provoking a fast dissolution of the previously formed calcite. Simultaneously, the $CSH_{2.5}$ dissolution continues. The summated effect of both dissolution processes results in a marked increase of material porosity. The effect of the degradation in the effective diffusivity is even more pronounced in this zone than in the previous one due to the effect of $CSH_{2.5}$ dissolution in the percolation exponent as described in Section 2.2.5.

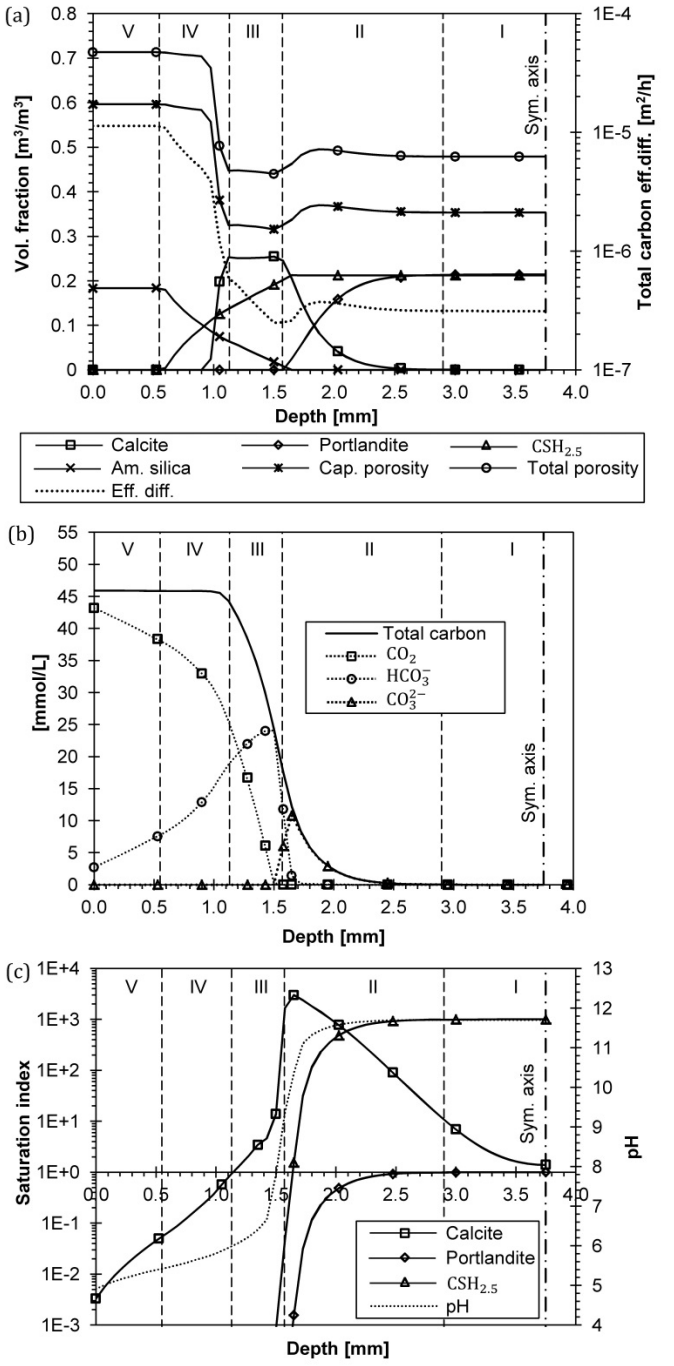

Fig. 6. Calculated radial profiles for Test A (pH 2.4 at 50 °C) after 15 days of exposition: (a) volumetric fractions and total carbon effective diffusivity; (b) carbon species; (c) saturation indexes and pH.

Finally, the fifth zone (V) corresponds to the completely degraded material, where the only remaining solids are the amorphous silicate hydrates and the inert CP (not plotted in Fig. 6a). Note that the diffusivity in this zone is two orders higher than the one in the unaltered zone.

In order to quantify the rate of advancement of the degradation, Duguid and Scherer visually identified in samples taken from the cement cylinders rings with different coloration, which were associated with different stages in the degradation process. In particular, a white ring developed in between the interior of the specimen and the practically completely decalcified outer corona. This white layer has been reported also by other authors (Kutchko et al., 2008; Liteanu and Spiers, 2011; Rimmelé et al., 2008) and associated with the presence of calcite and local reduction of the material porosity. In order to compare the measurements by Duguid and Scherer with our simulation results, a relationship need to be established between one (or more) model variable(s) and the fact that the material colour turned from grey to white. In this sense, it seems reasonable to relate the whitish colour to a certain threshold content of calcite. It has been found in the modelled tests that stablishing this threshold value in 0.22 m^3 of calcite per m^3 of material (5962 mol/m^3) leads to the best fitting with Duguid and Scherer measurements.

In Fig. 7, experimental and simulated penetration depths of the inner and outer sides of the white layer are plotted together as function of the exposure time for each testing condition. The penetration rates of both the inner and outer fronts of the white layer are well reproduced by the model in the four tested conditions, indicating that the effects of temperature and pH on the kinetics of cement paste degradation are well captured by the proposed formulation.

Preliminary sensitive analysis (not presented here) indicated that the rate of advancement of the decalcification front can only be capture if the increase of the effective diffusivity of the material due to the degradation of the material is considered. In the particular case of the proposed analytical Eq. (28), this effect could not be reproduced by only considering the increase of capillary porosity and, therefore, it was necessary to introduce a degradation law of the percolation coefficient (Eq. (29)). Final values of the percolation coefficient (n_f) ranging between 0.05 and 0.15, realistically capture the experimental results. Additionally, the same sensitive analysis indicated that the kinetic constants mainly determine the width of the degradation front, with minor effects on the advancement rate.

4. Concluding remarks

The assessing of the long-time performance of CO_2 storage in depleted oil fields requires to understand and to be able of predict the deterioration of well cements when exposed to carbonated brines.

With this aim in mind, a quantitative reactive-transport model is proposed in this paper. The model considers only four primary species, two with diffusion-reaction equations (calcium and total carbon) and two with only diffusion (chloride and alkalis). Secondary species are obtained from the primary ones by means of equilibrium equations. Solid dissolution and precipitation is treated with kinetic equations in all cases. The porosity and the effective diffusivity of the material are updated by tracking the volumetric evolution of the different solid species. A formula is proposed, based on the work of other authors (Oh and Jang, 2004), for estimating the effective diffusivity of the degraded material as a function of the volume fraction of solid species.

In the development of the formulation an effort has been made to limit the number of chemical species and reactions to the very minimum really necessary in order to reproduce the main aspects of the phenomenon relevant for assessing the

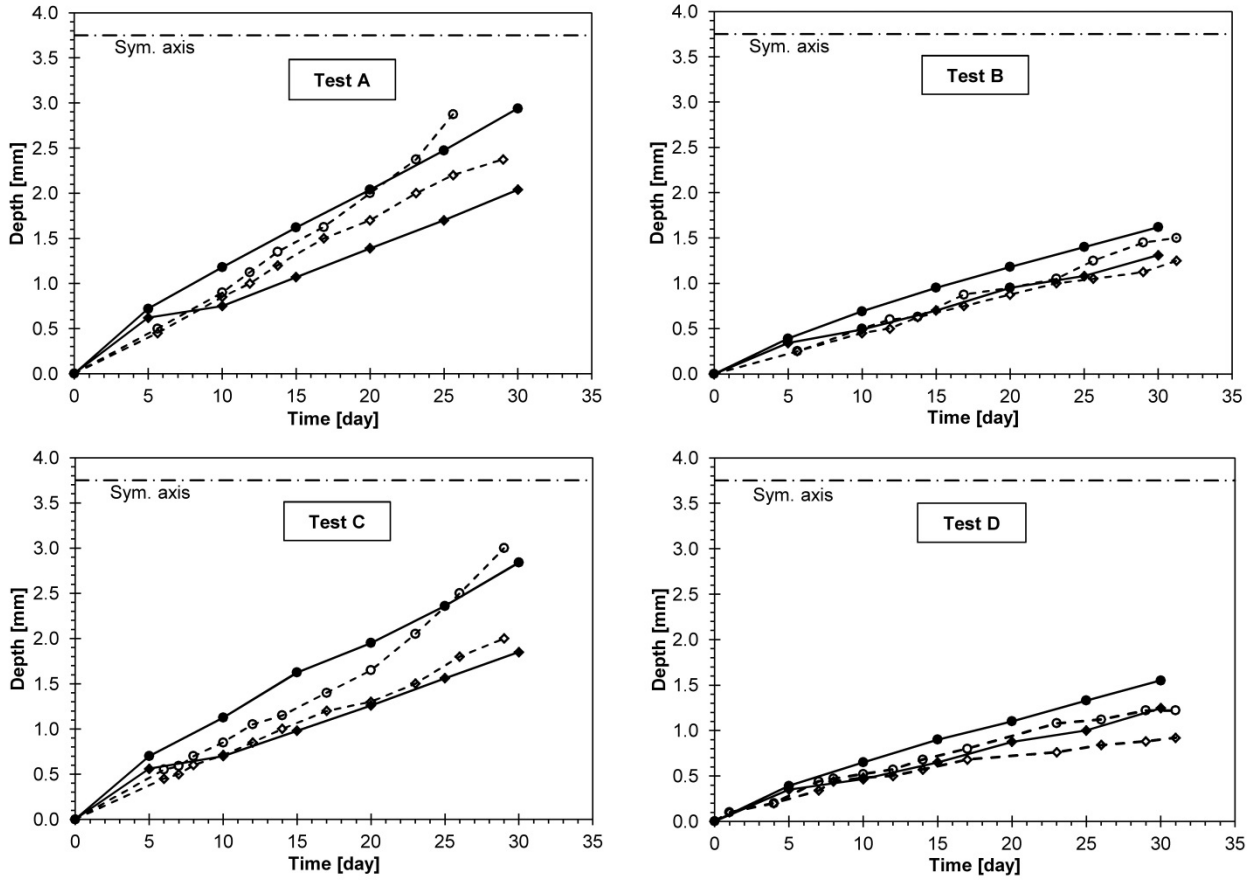

Fig. 7. Experimental and simulated reaction depth versus time for tests A (pH 2.4 and 50 °C), B (pH 2.4 and 20 °C), C (pH 3.7 and 50 °C) and D (pH 3.7 and 20 °C). Circles and diamonds indicate the inner and the outer limits of the white layer of the degradation front, respectively. Empty symbols indicate experimental results by Duguid and Scherer (2010), while solid symbols indicate simulation results.

evolution of the transport and mechanical parameters of the material.

The model has been benchmarked against laboratory experiments performed by Duguid and Scherer (2010) with cement pastes exposed to carbonated brines at different temperatures. Despite its relative simplicity, the model has been able of successfully reproducing both qualitative and quantitative experimental results.

Next steps in model development will consider coupling to mechanical degradation of the HCP and effects of cracks on diffusivity.

Acknowledgments

This research has been supported by MEC (Madrid) through project BIA2016-76543-R which includes European FEDER funds. The first author thanks the scholarship FPI (BES-2010-030515) from MEC (Madrid). The second author thanks the scholarship FI (2017FI_B00559) from AGAUR - Generalitat de Catalunya. Fruitful discussions and valuable comments from Dr. Andrés Idiart and his colleagues at Amphos 21 (Barcelona) are also acknowledged.

References

API Spec. 10A, 2002. Specification for Cements and Materials for Well Cementing, 23rd ed. Washington, DC, USA.

Börjesson, S., Emrén, A., Ekberg, C., 1997. A thermodynamic model for the calcium silicate hydrate gel, modelled as a non-ideal binary solid solution. Cement and Concrete Research 27, 1649–1657.

Brouwers, H., 2005. The work of Powers and Brownyard revisited: Part 2. Cement and Concrete Research 35, 1922–1936. doi:10.1016/j.cemconres.2005.04.009

Brouwers, H., 2004. The work of Powers and Brownyard revisited: Part 1. Cement and Concrete Research 34, 1697–1716. doi:10.1016/j.cemconres.2004.05.031

Brunet, J.P.L., Li, L., Karpyn, Z.T., Kutchko, B.G., Strazisar, B., Bromhal, G., 2013. Dynamic evolution of cement composition and transport properties under conditions relevant to geological carbon sequestration. Energy and Fuels 27, 4208–4220. doi:10.1021/ef302023v

Carey, J.W., Wigand, M., Chipera, S.J., WoldeGabriel, G., Pawar, R., Lichtner, P.C., Wehner, S.C., Raines, M.A., Guthrie, G.D., 2007. Analysis and performance of oil well cement with 30 years of CO2 exposure from the SACROC Unit, West Texas, USA. International Journal of Greenhouse Gas Control 1, 75–85. doi:10.1016/S1750-5836(06)00004-1

Chen, X., Wu, S., Zhou, J., 2013. Influence of porosity on compressive and tensile strength of cement mortar. Construction and Building Materials 40, 869–874. doi:10.1016/j.conbuildmat.2012.11.072

Duan, Z., Sun, R., 2003. An improved model calculating CO2 solubility in pure water and aqueous NaCl solutions from 273 to 533 K and from 0 to 2000 bar. Chemical Geology 193, 257–271. doi:10.1016/S0009-2541(02)00263-2

Duguid, A., Radonjic, M., Scherer, G.W., 2011. Degradation of cement at the reservoir/cement interface from exposure to carbonated brine. International Journal of Greenhouse Gas Control 5, 1413–1428. doi:10.1016/j.ijggc.2011.06.007

Duguid, A., Scherer, G.W., 2010. Degradation of oilwell cement due to exposure to carbonated brine. International Journal of Greenhouse Gas Control 4, 546–560. doi:10.1016/j.ijggc.2009.11.001

Fabbri, A., Jacquemet, N., Seyedi, D.M., 2012. A chemo-poromechanical model of oilwell cement carbonation under CO2 geological storage conditions. Cement and Concrete Research 42, 8–19. doi:10.1016/j.cemconres.2011.07.002

Gallucci, E., Zhang, X., Scrivener, K.L., 2013. Effect of temperature on the microstructure of calcium silicate hydrate (C-S-H). Cement and Concrete Research 53, 185–195. doi:10.1016/j.cemconres.2013.06.008

Gisby, J., Davies, R., 2007. CSH solubility modeling at different temperatures, in: 12th International Congress on the Chemistry of Cement, Cement Association of Canada. Montreal, Canada, pp. 1–12.

Huerta, N.J., Hesse, M.A., Bryant, S.L., Strazisar, B.R., Lopano, C., 2016. Reactive transport of CO2-saturated water in a cement fracture: Application to wellbore leakage during geologic CO2 storage. International Journal of Greenhouse Gas Control 44, 276–289. doi:10.1016/j.ijggc.2015.02.006

Huet, B.M., Prevost, J.H., Scherer, G.W., 2010. Quantitative reactive transport modeling of Portland cement in CO2-saturated water. International Journal of Greenhouse Gas Control 4, 561–574. doi:10.1016/j.ijggc.2009.11.003

Idiart, A.E., López, C.M., Carol, I., 2011a. Modeling of drying shrinkage of concrete specimens at the meso-level. Materials and Structures 44, 415–435. doi:10.1617/s11527-010-9636-2

Idiart, A.E., López, C.M., Carol, I., 2011b. Chemo-mechanical analysis of concrete cracking and degradation due to external sulfate attack: A meso-scale model. Cement and Concrete Composites 33, 411–423. doi:10.1016/j.cemconcomp.2010.12.001

IPCC, 2005. IPCC Special Report on Carbon Dioxide Capture and Storage. Prepared by Working Group III of the Intergovernmental Panel on Climate Change. Cambridge University Press, Cambridge, United Kingdom and New York, NY, USA.

Johannsen, K., Rademacher, S., 1999. Modelling the Kinetics of Calcium Hydroxide Dissolution in Water. Acta hydrochimica et hydrobiologica 27, 72–78.

Kestin, J., Khalifa, H.E., Correia, R.J., 1981. Tables of the dynamic and kinematic viscosity of aqueous NaCl solutions in the temperature range 20-150 °C and the pressure range 0.1-35 MPa. Journal of Physical and Chemical Reference Data. doi:10.1063/1.555641

Kutchko, B.G., Strazisar, B.R., Dzombak, D. a., Lowry, G. V., Thauiow, N., 2007. Degradation of well cement by CO2 under geologic sequestration conditions. Environmental Science & Technology 41, 4787–4792. doi:10.1021/es062828c

Kutchko, B.G., Strazisar, B.R., Lowry, G.V., Dzombak, D. a., Thaulow, N., 2008. Rate of CO2 Attack on Hydrated Class H Well Cement under Geologic Sequestration Conditions. Environmental Science & Technology 42, 6237–6242. doi:10.1021/es800049r

Liaudat, J., López, C.M., Carol, I., 2016. Numerical and Experimental study of ASR in concrete at the meso-level, in: Saouma, V., Bolander, J., Landis, E. (Eds.), The 9th International Conference on Fracture Mechanics of Concrete and Concrete Structures (FraMCoS 9). doi:10.21012/FC9.287

Lide, D.R. (Ed.), 2004. CRC Handbook of Chemistry and Physics, 85th ed. CRC Press, Boca Raton (FL).

Liteanu, E., Spiers, C.J., 2011. Fracture healing and transport properties of wellbore cement in the presence of supercritical CO2. Chemical Geology 281, 195–210. doi:10.1016/j.chemgeo.2010.12.008

Muller, A.C.A., Scrivener, K.L., Gajewicz, A.M., McDonald, P.J., 2013. Use of bench-top NMR to measure the density, composition and desorption isotherm of C-S-H in cement paste. Microporous and Mesoporous Materials 178, 99–103. doi:10.1016/j.micromeso.2013.01.032

Muller, A.C.A., Scrivener, K.L., Gajewicz, A.M., McDonald, P.J., 2013. Densification of C-S-H measured by 1H NMR relaxometry. Journal of Physical Chemistry C 117, 403–412. doi:10.1021/jp3102964

Oh, B.H., Jang, S.Y., 2004. Prediction of diffusivity of concrete based on simple analytic equations. Cement and Concrete Research 34, 463–480. doi:10.1016/j.cemconres.2003.08.026

Pitzer, K.S. (Ed.), 1991. Activiy coefficients in electrolyte solutions, 2nd ed. CRC Press, Boca Raton (FL).

Powers, T., Brownyard, T., 1946. Studies of the physical properties of hardened Portland cement paste. ACI Journal Proceedings 43, 101–132, 249–336, 469–505, 549–602, 669–712, 845–8.

Rahman, M.M., Nagasaki, S., Tanaka, S., 1999. A model for dissolution of CaO-SiO2-H2O gel at Ca/Si >1. Cement and Concrete Research 29, 1091–1097.

Raoof, A., Nick, H.M., Wolterbeek, T.K.T., Spiers, C.J., 2012. Pore-scale modeling of reactive transport in wellbore cement under CO2 storage conditions. International Journal of Greenhouse Gas Control 11S, S67–S77. doi:10.1016/j.ijggc.2012.09.012

Rimmelé, G., Barlet-Gouédard, V., Porcherie, O., Goffé, B., Brunet, F., 2008. Heterogeneous porosity distribution in Portland cement exposed to CO2-rich fluids. Cement and Concrete Research 38, 1038–1048. doi:10.1016/j.cemconres.2008.03.022

Rodriguez, M., López, C.M., Carol, I., 2017. Modelling of heat and moisture transfer in concrete at high temperature, in: Oñate, E., Owen, D.R.J., Peric, D., Chiumenti, M. (Eds.), Computational Plasticity XIV – Fundamentals and Applications. International Center for Numerical Methods in Engineering (CIMNE), Barcelona, Spain, pp.

732–741.
Samson, E., Lemaire, G., 1999. Modeling chemical activity effects in strong ionic solutions. Computational Materials Science 15, 285–294.
Samson, E., Marchand, J., 2007. Modeling the effect of temperature on ionic transport in cementitious materials. Cement and Concrete Research 37, 455–468. doi:10.1016/j.cemconres.2006.11.008
Shen, J., 2011. Reactive Transport Modeling of CO2 through Cementitious Materials under CO2 Geological Storage Conditions. doi:10.1002/9781118577424.ch10
Shen, J., Dangla, P., Thiery, M., 2013. Reactive transport modeling of CO2 through cementitious materials under CO2 geological storage conditions. International Journal of Greenhouse Gas Control 18, 75–87. doi:10.1016/j.ijggc.2013.07.003
SPE, 2016. Cement composition and classification [WWW Document]. PetroWiki (Society of Petroleum Engineers). URL http://petrowiki.org/Cement_composition_and_classification#cite_note-r3-3 (accessed 7.25.16).
Talman, S.J., Wiwchar, B., Gunter, W.D., 1990. Dissolution kinetics of calcite in the H2O-CO2 system along the steam saturation curve to 210°C. Fluid-Mineral Interactions: A Tribute to H. P. Eugster 41–55.
THERMODDEM, 2014. Thermochemical and Mineralogical Tables for Geochemical Modeling [WWW Document]. Bureau de Recherches Géologiques et Minières. URL http://thermoddem.brgm.fr (accessed 7.11.16).
Trapote-Barreira, A., Cama, J., Soler, J.M., 2014. Dissolution kinetics of C–S–H gel: Flow-through experiments. Physics and Chemistry of the Earth 70–71, 17–31. doi:10.1016/j.pce.2013.11.003
Walsh, S.D.C., Du Frane, W.L., Mason, H.E., Carroll, S.A., 2013. Permeability of Wellbore-Cement Fractures Following Degradation by Carbonated Brine. Rock Mechanics and Rock Engineering 46, 455–464. doi:10.1007/s00603-012-0336-9
Yuan-Hui, L., Gregory, S., 1974. Diffusion of ions in sea water and in deep-sea sediments. Geochimica et cosmochimica acta 38, 703–714.
Zhang, Y., Dawe, R., 1998. The kinetics of calcite precipitation from a high salinity water. Applied Geochemistry 13, 85–95. doi:10.1016/s0883-2927(97)00061-9